

Coherent cyclotron motion beyond Kohn's theorem

T. Maag¹, A. Bayer¹, S. Baierl¹, M. Hohenleutner¹, T. Korn¹, C. Schüller¹,

D. Schuh¹, D. Bougeard¹, C. Lange^{1*}, and R. Huber¹

¹*Department of Physics, University of Regensburg, 93040 Regensburg, Germany*

M. Mootz², J. E. Sipe^{2,3}, S. W. Koch², and M. Kira²

²*Department of Physics, University of Marburg, 35032 Marburg, Germany*

³*Department of Physics and Institute for Optical Sciences, University of Toronto, 60 St. George St.,*

Toronto, Ontario, Canada

**christoph.lange@physik.uni-regensburg.de*

In solids, the high density of charged particles makes many-body interactions a pervasive principle governing optics and electronics¹⁻¹². However, Walter Kohn found in 1961 that the cyclotron resonance of Landau-quantized electrons is independent of the seemingly inescapable Coulomb interaction between electrons². While this surprising theorem has been exploited in sophisticated quantum phenomena¹³⁻¹⁵ such as ultrastrong light–matter coupling¹⁶, superradiance¹⁷, and coherent control¹⁸, the complete absence of nonlinearities excludes many intriguing possibilities, such as quantum-logic protocols¹⁹. Here, we use intense terahertz pulses to drive the cyclotron response of a two-dimensional electron gas beyond the protective limits of Kohn's theorem. Anharmonic Landau ladder climbing and distinct terahertz four- and six-wave mixing signatures occur, which our theory links to dynamic Coulomb effects between electrons and the positively charged ion background. This new context for Kohn's theorem unveils previously inaccessible internal degrees of freedom of Landau electrons, opening up new realms of ultrafast quantum control for electrons.

Controlling superpositions of electronic quantum states has been a paradigm of fundamental physics and quantum-information technology¹⁹. Sophisticated protocols have been implemented in atomic gases²⁰ whereas solids represent a more challenging environment due to complicated many-body

interactions. Quantum manipulation has been quite successful in atom-like single-particle systems, such as quantum dots²¹ while controlling interacting many-body systems is still in its infancy. Following Lev Landau's suggestion to combine collective properties of an interacting particle system into quasiparticles¹, researchers effectively analyse crystal electrons and holes^{4,5}, excitons^{6,9}, dropletions¹¹, polarons⁷, magnons²² or Cooper pairs¹². In particular, ultrashort pulses in the terahertz (1 THz = 10^{12} Hz) spectral range have become a powerful tool to probe^{4,6,7,12,17} and control^{8,18,22,23} quasiparticle excitations, such as intra-excitonic transitions⁶ or superconductor Higgs bosons¹².

For most quasiparticle excitations, Coulomb scattering leads to coherence times in the range of a few to a few hundred femtoseconds, which is too short for most quantum-logic operations. However, the cyclotron resonance (CR) in a two-dimensional electron gas (2DEG) represents a unique exception^{2,13-18}. In a magnetically biased 2DEG, Landau electrons emerge as elementary quasiparticles. According to Kohn's theorem the quantisation energy of the harmonic spectrum of Landau levels (LLs) defined by the cyclotron frequency ν_c is inert to Coulomb scattering². Although the absence of Coulomb complications warrants a long-lived CR coherence, the accompanying perfectly harmonic behavior has an apparent downside: Multiphoton excitations drive perfect Landau electrons only to climb up the LLs, preventing Rabi flopping, which is the desired elementary process in many quantum-logic operations¹⁹.

Here, we investigate the possibility to induce a distinctly anharmonic CR response with the goal to coherently control transitions among few singled-out LLs. Intense THz pulses coherently drive the state of a 2DEG up the Landau ladder by as much as six rungs within a single cycle of the carrier wave and induce anharmonicities which render LL transitions distinguishable. Furthermore, strong coherent nonlinearities, such as four- and six-wave mixing signals are observed. While Kohn's theorem has been violated via phonons^{24,25}, nonparabolic electron dispersion²⁶, or in a Bose-Einstein condensate close to a Feshbach resonance²⁷, our experiment-theory comparison unambiguously reveals a nonlinear response that stems from the Coulomb interaction itself, between the electrons and the ionic background.

Our sample hosts two 30-nm wide n-doped GaAs quantum wells (QWs) (see Methods), each containing a 2DEG. To calibrate the system, phase-locked low-amplitude ($\mathcal{E}_0 = 90 \text{ V/cm}$) THz pulses are transmitted through the structure. Polarization components parallel (\mathcal{E}_x) and perpendicular (\mathcal{E}_y) to the incident pulses are separately detected by electro-optic sampling (EOS), as a function of delay time t (Fig. 1a). Without magnetic bias, $\mathcal{E}_x(t)$ (Fig. 1c, black curve) closely follows the incident waveform (Supplementary Discussion 1). When a magnetic bias $B = 3.5 \text{ T}$ is applied perpendicularly to the 2DEG plane, long-lived trailing oscillations emerge due to the CR with $\nu_c = 1.45 \text{ THz}$ (Fig. 1c, blue curve)¹⁸. Here the weak THz field induces a polarization between LLs $|n = 0\rangle$ (filling factor $f = 0.95$) and $|n = 1\rangle$ (Fig. 1b), reemitting a circularly polarized THz wave (Fig. 1c, inset) whose coherence time $\tau_c = 9 \text{ ps}$ is likely limited by superradiant decay¹⁷.

We then drive the calibrated system with intense THz pulses generated by tilted-pulse-front optical rectification²³. The amplitude of the reemitted field $\mathcal{E}_y(t)$ (Fig. 2a) increases with \mathcal{E}_0 , but the temporal waveform remains similar up to $\mathcal{E}_0 = 1.4 \text{ kV/cm}$. For $\mathcal{E}_0 \geq 2.9 \text{ kV/cm}$, the trailing oscillations slow down and decay more rapidly until the inter-LL polarization essentially follows the driving field, for $\mathcal{E}_0 = 8.7 \text{ kV/cm}$, as the coherence decays almost instantly. The spectrum of the reemitted field (Fig. 2b), which is initially centred at $\nu_c = 1.45 \text{ THz}$, red-shifts and broadens with increasing \mathcal{E}_0 until its shape converges to the spectrum of the driving pulse. This pronounced field dependence is irreconcilable with the linear response of a harmonic oscillator, indicating that the cyclotron transition is driven into a strongly nonlinear regime by the intense THz transients. Figure 2c shows the dephasing time τ_c as a function of the THz amplitude \mathcal{E}_0 . Starting at a low-field value of $\tau_c = 9 \text{ ps}$, the decay time drops abruptly for $\mathcal{E}_0 > 3 \text{ kV/cm}$, and ultimately approaches $\tau_c = 0.5 \text{ ps}$.

Kohn's theorem implies that the purely repulsive electron–electron Coulomb interaction cannot produce observable nonlinearities in a 2DEG. However, in a real modulation-doped system, the 2DEG always resides on a positive background charge that holds the electrons together as a homogeneous gas by preventing the formation of a Wigner crystal²⁸ or the escape of electrons to the edges of the sample. Since the attractive electron–ion interaction is not limited by Kohn's theorem, it can indeed induce CR nonlinearities.

The experiments are analyzed with cluster-expansion-based many-body computations³ including the nonparabolic dispersion of Landau electrons, their coupling to THz fields as well as phonons, and the Coulombic electron–electron and electron–ion interaction. Technically, a_λ (a_λ^\dagger) annihilates (creates) an electron in a LL λ such that $p_v^\lambda = \langle a_\lambda^\dagger a_v \rangle$ identifies both microscopic polarization ($\lambda \neq v$) and electron distributions ($\lambda = v$) among different LLs. The THz excitation yields an exact quantum dynamics defined by the semiconductor Bloch equations (SBEs)³

$$i\hbar \frac{\partial}{\partial t} p_v^\lambda = E_v^\lambda p_v^\lambda + \sum_s (\Omega_s^v p_s^\lambda - \Omega_\lambda^s p_v^s) + C_v^\lambda + D_v^\lambda \quad (1)$$

where E_v^λ is the transition energy between two LLs with a dipole \mathbf{d}_v^λ , and $\Omega_v^\lambda \equiv \mathbf{d}_v^\lambda \cdot \boldsymbol{\varepsilon}_0$ is the Rabi energy of the THz field. The Coulomb interaction renormalizes both E_v^λ and Ω_v^λ , and introduces a contribution C_v^λ whose electron–electron (electron–ion) part contains a repulsive (attractive) Coulomb matrix element V (W) between four LLs (LLs and ions), yielding Coulomb sums of type $\sum_{j,s,u} V_{u,j}^{v,s} p_u^s p_j^\lambda$ and $\sum_j W_\lambda^j p_v^j$. Besides these Hartree-Fock contributions, the SBEs couple to two-particle correlations^{3,29}, inducing phonon scattering and excitation-induced dephasing (EID) stemming from Coulomb scattering of polarization with excited electrons^{3,29,30}. Longitudinal optical phonons efficiently dephase polarization involving LLs with energy above $\hbar\omega_{LO} = 36$ meV, and the EID is described with an excitation-dependent model explained in Supplementary Discussion 10.

The principal quantum number n of a LL $\lambda = (n, l)$ defines its energy while an additional quantum number l defines angular momentum and introduces infinite degeneracy among LLs. We use 1500 LLs in solving Eq. (1), which is shown to yield a converged macroscopic response (Supplementary Discussion 8). The SBEs then contain 10^{10} Coulomb-sum calculations at each time step, rendering simulations extremely demanding. Nevertheless, our computations include even the principal EID effects; at low excitations, all l states are occupied evenly such that the Coulombic in- and out-scattering fully compensate each other, yielding vanishing EID. However, strong THz excitations generate peaks in the l distribution, unbalancing the Coulomb scattering and yielding detectable EID proportional to the density of excited electrons.

Figure 2d compares the transmitted field \mathcal{E}_y for $\mathcal{E}_0 = 0.7$ kV/cm and 5.7 kV/cm as obtained from our full theory (solid curves) with the results computed without Coulomb interaction (dashed curves) and a classical calculation with a nonparabolic band and constant τ_c (shaded area). The weak-intensity result ($\mathcal{E}_0 = 0.7$ kV/cm) is well reproduced by all theoretical models, verifying the applicability of Kohn's theorem in this case. However, for the stronger field $\mathcal{E}_0 = 5.7$ kV/cm, only the full quantum theory can reproduce the experimental decay of \mathcal{E}_y and the redshift of ν_c . As in the experiment, the indicated oscillation minimum of \mathcal{E}_y (red vertical line) is delayed by 0.1 ps with respect to the position expected for constant $\nu_c = 1.45$ THz (blue vertical line), which manifests a violation of Kohn's theorem. Even though the simplified models neglect Coulomb interaction, they do yield a change of ν_c implying that the nonparabolic dispersion contributes to the softening of the CR. However, they predict incorrect decay dynamics because the classical computation lacks the phase diffusion among LLs, present in the quantum calculations.

Our full theory also explains the threshold-like onset of dephasing above $\mathcal{E}_0 = 3$ kV/cm (Fig. 2c, red solid line) attributing this effect to an efficient population transfer. While low THz amplitudes (0.7 kV/cm) excite only a few percent of charge carriers into LL $|n = 1\rangle$ (Fig. 2e, blue bars), strong pulses drive coherent ladder climbing. At $\mathcal{E}_0 = 4.3$ kV/cm (violet bars), more than half of the electrons are excited and distributed up to $|n = 6\rangle$ where rapid dephasing and relaxation by LO phonon emission sets in. The THz-induced population transfer is faster than relaxation such that even LLs above the LO phonon energy are populated. Remarkably, THz transients with $\mathcal{E}_0 = 8.7$ kV/cm (red bars) largely depopulate $|n = 0\rangle$ and prepare a compact superposition of eigenstates, peaking at $|n = 5\rangle$. This wavepacket rapidly loses its coherence because 25% of its weight is located above the phonon energy. Thus, the abrupt onset of dephasing above $\mathcal{E}_0 = 3$ kV/cm arises from the combination of a compact wavepacket distribution and a sharp threshold for phonon scattering. Furthermore, the experiment corroborates that coherent state inversion works even for a massive many-body system and corresponding LLs should be well-suited for coherent quantum control.

To test these perspectives systematically, two phase-locked THz pulses A and B, polarized in x- and y-directions, respectively, are focused onto the sample for field-resolved two-dimensional (2D) THz

spectroscopy. The transmitted total THz field is resolved in amplitude and phase as a function of EOS time, t , and the delay between the two incident pulses, τ (Fig. 3a). Subsequently, the response to individual pulses A and B is subtracted to isolate the nonlinear polarization induced by both pulses $\mathcal{E}_{NL}(t, \tau)$,^{31,32} which vanishes for a strictly harmonic CR. In contrast, Figs. 3b-e show strong nonlinear signals $\mathcal{E}_{NL}(t, \tau)$ for all peak amplitudes between $\mathcal{E}_A = 1.4$ kV/cm and 5.7 kV/cm while $\mathcal{E}_B = 90$ V/cm is kept constant. Constant-phase lines of pulse B appear vertically in the 2D data maps whereas the phase fronts of pulse A occur under a 45° angle (see Supplementary Discussion 3).

For $\mathcal{E}_A = 1.4$ kV/cm (Fig. 3b), \mathcal{E}_{NL} is strongly modulated along τ with a period $\Delta\tau_1 = 1/\nu_c = 0.69$ ps evidencing that the nonlinear interaction is coherently mediated by ν_c . This feature persists even when the incident pulses do not overlap in time since the coherence is stored in the LL system. For larger \mathcal{E}_A (Figs. 3c-e), an additional modulation with a period of $\Delta\tau_2 = 2/\nu_c = 0.34$ ps, corresponding to twice the cyclotron frequency, emerges and becomes dominant for $\mathcal{E}_A = 4.3$ kV/cm. Increasing the field to $\mathcal{E}_A = 5.7$ kV/cm (Fig. 3e) accelerates decoherence, leaving only weak modulations during temporal overlap of both pulses, around $t + \tau = 0$. Supplementary Discussion 2 shows similar results for a single-well structure, demonstrating the universality of these nonlinearities.

A 2D Fourier transformation allows us to disentangle different nonlinear optical processes contributing to $\mathcal{E}_{NL}(t, \tau)$. Figures 3h-k display the spectral amplitude as a function of the frequencies ν_t and ν_τ associated with the EOS time and the relative delay between the pulses, respectively^{31,32}. Several distinct maxima occur at integer multiples of ν_c : The peak located at $(\nu_t, \nu_\tau) = (\nu_c, 0)$ (Fig. 3h, arrow ' k_{p1} ') represents a pump-probe signal where pulse A (B) acts as a pump (probe) pulse, whereas the maximum at $(\nu_c, -\nu_c)$ (arrow ' k_{p2} ') is a pump-probe signal for which pulse A and B switch their roles. In addition, strong four-wave-mixing (FWM, ' k_{41} ', ' k_{42} ') emerges. As \mathcal{E}_A is increased to 2.9 kV/cm (Fig. 3i), the FWM signal at k_{42} (red circle) surpasses the diagonal pump-probe signal k_{p2} in amplitude. Even six-wave mixing (SWM, ' k_{61} ', orange circle) occurs. For $\mathcal{E}_A = 4.3$ kV/cm (Fig. 3j), FWM is the dominant contribution at non-zero ν_τ and explains the $\Delta\tau_2$ -periodic response in the time-domain (Fig. 3d). Finally, the strongly reduced coherence time for $\mathcal{E}_A = 5.7$ kV/cm (Fig. 3k) suppresses wave-mixing processes, and the incoherent pump-probe signal at k_{p1} dominates.

To identify the origin of these nonlinearities, we apply our many-body theory to the 2D scenario using the experimental THz waveforms. The time-domain data of the full calculation for weak ($\mathcal{E}_A = 1.4$ kV/cm, Fig. 3f) and strong ($\mathcal{E}_A = 4.3$ kV/cm, Fig. 3g) pulses explain our experiment, reproducing the $\Delta\tau_1$ - and $\Delta\tau_2$ -periods in $\mathcal{E}_{NL}(t, \tau)$, as well as their relative weights and decay. Correspondingly, the frequency maps (Figs. 3l, m) exhibit multi-wave mixing features in quantitative agreement with the experiment.

The nonlinearities are a consequence of the breakdown of the translational invariance and thus a violation of Kohn's theorem which follows either from the nonparabolic electron dispersion or intrinsic Coulomb-interaction effects. A switch-off analysis allows us to determine the microscopic origin of nonlinearities. Figure 4 shows slices of \mathcal{E}_{NL} at constant $t = 3.3$ ps (see Figs. 3f, g, vertical lines). For $\mathcal{E}_A = 1.4$ kV/cm (Fig. 4a), the $\Delta\tau_1$ -period dominates the dynamics of $\mathcal{E}_{NL}(\tau)$. When the nonparabolicity is switched off (red line), \mathcal{E}_{NL} is strongly suppressed. However, eliminating Coulomb effects (dashed line) yields almost unchanged \mathcal{E}_{NL} , revealing the nonparabolic band structure as the dominant nonlinearity for low fields. For $\mathcal{E}_A = 4.3$ kV/cm (Fig. 4b), the nonlinear response is almost one order of magnitude stronger than for $\mathcal{E}_A = 1.4$ kV/cm. Now the parabolic band approximation (red line) produces virtually the same result as the full computation (black line), showing that the Coulomb interaction dominates \mathcal{E}_{NL} for strong fields. Further insights to the intriguing Coulomb effects are gained by computing $\mathcal{E}_{NL}(\tau)$ without EID (dashed line, see Supplementary Discussion 10); only the computation with EID explains the experiment, which indicates new possibilities to utilize ultrafast nonlinear switching and decay channels.

Lifting the protection of Kohn's theorem through non-perturbative excitations of a Landau system opens the door to a rich spectrum of nonlinearities, fine-tuned by the THz driving field. High-order nonlinear processes promoted by the intrinsically large dipole moments of the cyclotron resonance hold the prospect for THz quantum control, even at low field amplitudes. Future quantum logic devices may combine cyclotron transitions with metamaterials to further lower the required field amplitude and the footprint of a single qubit. On-chip electronic THz sources may even pave the way towards scalable all-electrical quantum devices. Generally, the principle of accessing internal degrees

of freedom in a many-body quantum system through Coulomb correlations suggests that the role of massive many-body interactions, thus far considered detrimental to quantum control, will have to be reassessed.

- [1] Landau, L. Theory of Fermi-liquids. *Soviet Phys. JETP* **3**, 920 (1957).
- [2] Kohn, W. Cyclotron Resonance and de Haas-van Alphen Oscillations of an Interacting Electron Gas. *Phys. Rev.* **123**, 1242 (1961).
- [3] Kira, M., & Koch, S. W. *Semiconductor Quantum Optics*. Cambridge University Press (2011).
- [4] Huber, R. et al. How many-particle interactions develop after ultrafast excitation of an electron-hole plasma. *Nature* **414**, 286-289 (2001).
- [5] Chemla, D. S. & Shah J. Many-body and correlation effects in semiconductors. *Nature* **411**, 549-557 (2001).
- [6] Kaindl, R. A., Carnahan, M. A., Haegele, D., Lovenich, R., & Chemla, D. S. Ultrafast terahertz probes of transient conducting and insulating phases in an electron-hole gas. *Nature* **423**, 734-738 (2003).
- [7] Gaal, P. et al. Internal motions of a quasiparticle governing its ultrafast nonlinear response. *Nature* **450**, 1210-1213 (2007).
- [8] Leinß, S. et al. Terahertz coherent control of optically dark paraexcitons in Cu₂O. *Phys. Rev. Lett.* **101**, 246401 (2008).
- [9] Turner, D. B., Nelson, K. A. Coherent measurements of high-order electronic correlations in quantum wells. *Nature* **466**, 1089–1092 (2010).
- [10] Rice, W. et al. Observation of Forbidden Exciton Transitions Mediated by Coulomb Interactions in Photoexcited Semiconductor Quantum Wells. *Phys. Rev. Lett.* **110**, 137404 (2013).
- [11] Almand-Hunter, A. et al. Quantum droplets of electrons and holes. *Nature* **506**, 471–475 (2014).
- [12] Matsunaga, R. et al. Light-induced collective pseudospin precession resonating with Higgs mode in a superconductor. *Science* **345**, 1145 (2014).

- [13] Timothy Noe II, G. et al. Giant superfluorescent bursts from a semiconductor magneto-plasma. *Nature Phys.* **8**, 219-224 (2012).
- [14] Wang X., Belyanin, A. A., Crooker, S. A., Mittleman, D. M., & Kono, J., Interference-induced terahertz transparency in a semiconductor magneto-plasma. *Nature Phys.* **6**, 126-130 (2010).
- [15] Kukushkin, I. V., Smet, J. H., von Klitzing, K. & Wegscheider, W. Cyclotron resonance of composite fermions. *Nature* **415**, 409-412 (2002).
- [16] Scalari, G. et al. Ultrastrong Coupling of the Cyclotron Transition of a 2D Electron Gas to a THz Metamaterial. *Science* **335**, 1323-1326 (2012).
- [17] Zhang, Q. et al. Superradiant Decay of Cyclotron Resonance of Two-Dimensional Electron Gases. *Phys. Rev. Lett.* **113**, 047601 (2014).
- [18] Arikawa, T. et al. Quantum control of a Landau-quantized two-dimensional electron gas in a GaAs quantum well using coherent terahertz pulses. *Phys. Rev. B* **84**, 241307(R) (2011).
- [19] Ladd, T. D. et al. Quantum computers. *Nature* **464**, 45-53 (2010).
- [20] Wieman, C. E., Pritchard, D. E., & Wineland, D. J., Atom cooling, trapping, and quantum manipulation. *Rev. Mod. Phys.* **71**, S253 (1999).
- [21] Press, D., Ladd, T. D., Zhang, B., & Yamamoto, Y. Complete quantum control of a single quantum dot spin using ultrafast optical pulses. *Nature* **456**, 218-221 (2008).
- [22] Kampfrath, T. et al. Coherent terahertz control of antiferromagnetic spin waves. *Nature Photon.* **5**, 31-34 (2011).
- [23] Kampfrath, T., Tanaka, K., & Nelson, K. A. Resonant and nonresonant control over matter and light by intense terahertz transients. *Nature Photon.* **7**, 680-690 (2013).
- [24] Hu, C. M., Batke, E., Köhler, K., & Ganser, P., Interaction Coupled Cyclotron Transitions of Two-Dimensional Electron Systems in GaAs at High Temperatures, *Phys. Rev. Lett.* **75**, 918 (1995)

- [25] Hu, C. M., Batke, E., Köhler, K., & Ganser, P., Resonant Polaron Coupling of High Index Electron Landau Levels in GaAs Heterostructures. *Phys. Rev. Lett.* **76**, 1904 (1996).
- [26] Mittendorf, M., et al. Carrier dynamics in Landau-quantized graphene featuring strong Auger scattering. *Nature Phys.* **11**, 75–81 (2015).
- [27] Al-Jibbouri, H. & Pelster, A. Breakdown of the Kohn theorem near a Feshbach resonance in a magnetic trap. *Phys. Rev. A.* **88**, 033621 (2013).
- [28] Ghosal, A., Güçlü, A.D., Umrigar, C.J., Ullmo, D., & Baranger, H. U. Correlation-induced inhomogeneity in circular quantum dots. *Nature. Phys.* **2**, 336—340 (2006).
- [29] Kira, M. & Koch, S. W. Many-body correlations and excitonic effects in semiconductor spectroscopy. *Prog. Quantum Electron.* **30**, 155 (2006).
- [30] Smith, R. P. *et al.* Extraction of many-body configurations from nonlinear absorption in semiconductor quantum wells. *Phys. Rev. Lett.* **104**, 247401 (2010).
- [31] Kuehn, W. Reimann, K. Woerner, M. & Elsaesser, T. Phase-resolved two-dimensional spectroscopy based on collinear n-wave mixing in the ultrafast time domain. *J. Chem. Phys.* **130**, 164503 (2009).
- [32] Junginger, F. et al. Nonperturbative Interband Response of a Bulk InSb Semiconductor Driven Off Resonantly by Terahertz Electromagnetic Few-Cycle Pulses. *Phys. Rev. Lett.* **109**, 147403 (2012).

Acknowledgements The work in Regensburg was supported by the European Research Council through grant no. 305003 (QUANTUMsubCYCLE) and the Deutsche Forschungsgemeinschaft (LA 3307/1-1, HU 1598/2-1, BO 3140/3-1, and collaborative research center SFB 689). The work at the University of Marburg was supported by the Deutsche Forschungsgemeinschaft through SFB 1083 and grant KI 917/2-2 (M.K.), and the Alexander von Humboldt foundation (J.S.).

Author contributions T.M., A.B. M.M. and C.L. contributed equally to this work. C.L., T.M., M.K., S.W.K. and R.H. conceived the study. T.M., C.L., A.B., S.B., M.H., T.K., C.S., D.B. and R.H. carried out the experiment and analysed the data. A.B., D.S. and D.B. prepared the sample. M.M., J. S., S.W.K. and M.K. developed the quantum-mechanical model and carried out the computations. C.L., T.M., M.M., S.W.K., M.K. and R.H. wrote the manuscript. All authors discussed the results.

Additional information

Correspondence and requests for materials should be addressed to C.L.

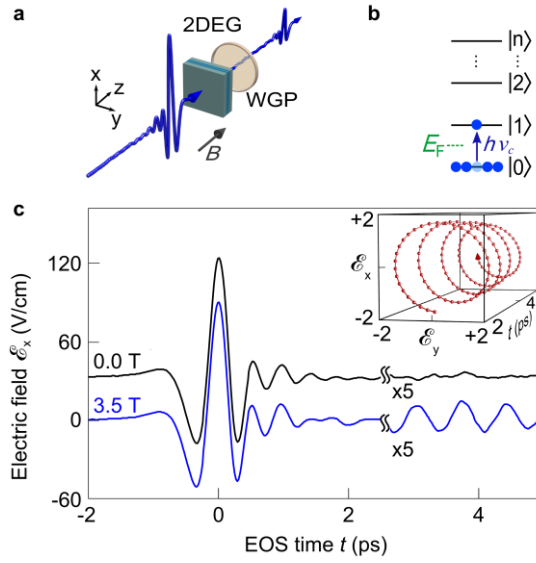


Figure 1 | Linear THz magnetospectroscopy of a 2DEG Landau system. **a**, Schematic of time-domain THz setup in Faraday geometry. Linearly polarized THz transients drive inter-Landau level transitions in two 30-nm wide, n-doped GaAs QWs. The transmitted waveforms are detected via electro-optic sampling (EOS) in a ZnTe crystal with polarization selectivity achieved through a wire-grid polarizer (WGP). **b**, Landau level scheme. At $B = 3.5$ T, all electrons condense to the first Landau state $|n = 0\rangle$ with a filling factor of $f = 0.95$. **c**, Transmitted THz pulses at $B = 3.5$ T (blue curve) and $B = 0$ T (black curve, offset for clarity). For $B = 3.5$ T, trailing oscillations result from the decay of the polarization, which our low-field THz transient excites solely between LLs $|n = 0\rangle$ and $|n = 1\rangle$. Inset: Polarization-resolved plot of the reemission showing its circular nature.

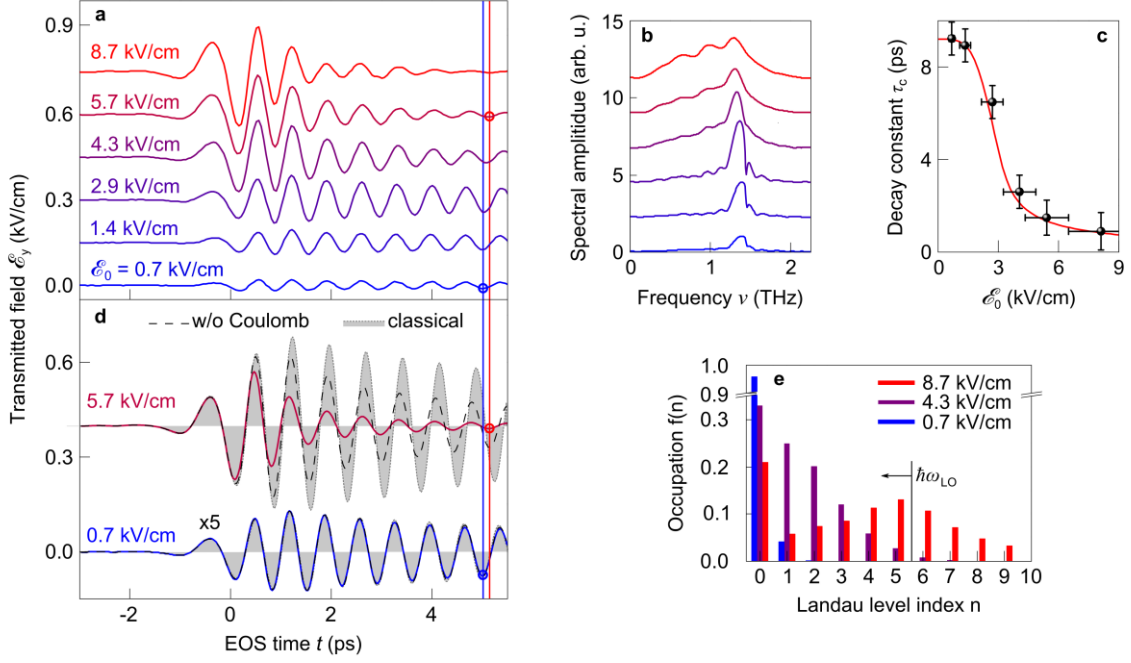


Figure 2 | Dynamics of Landau system under nonperturbative single-pulse excitation. a, Waveform of the transmitted field \mathcal{E}_y for various amplitudes \mathcal{E}_0 of the incident THz transient (polarized in x-direction), vertically offset for clarity. Vertical lines indicate the temporal position of a local minimum of \mathcal{E}_y for low-field excitation ($\mathcal{E}_0 = 0.7$ kV/cm, vertical blue line) and high-field excitation ($\mathcal{E}_0 = 5.7$ kV/cm, vertical red line), indicating a field-induced phase retardation. **b,** Fourier transform of \mathcal{E}_y from **a** evidencing the broadening and red-shift of the cyclotron resonance from 1.45 to 1.3 THz. **c,** Coherence time τ_c extracted from fitting the waveforms $\mathcal{E}_y(t)$ in **a** with an exponentially decaying sinusoidal function (black dots), and calculation (red line). Vertical and horizontal error bars mark the standard deviation intervals ($\pm\sigma$) for the fit and for the THz amplitude, respectively, the latter arising from uncertainties in the THz spot size and power. **d,** THz dynamics calculated with a full quantum theory for $\mathcal{E}_0 = 0.7$ kV/cm (blue curve) and $\mathcal{E}_0 = 5.7$ kV/cm (red curve). Dashed curves: quantum theory neglecting Coulomb interaction, shaded areas: classical theory including the band nonparabolicity of GaAs. **e,** Bar chart of calculated Landau level population as a function of LL index n at a fixed delay time $t = 0.6$ ps, for $\mathcal{E}_0 = 0.7$ kV/cm (blue bars), $\mathcal{E}_0 = 4.3$ kV/cm (violet bars) and $\mathcal{E}_0 = 8.7$ kV/cm (red bars). Phonon scattering sets in for energies above the LO phonon energy $\hbar\omega_{LO}$ (vertical black line and arrow).

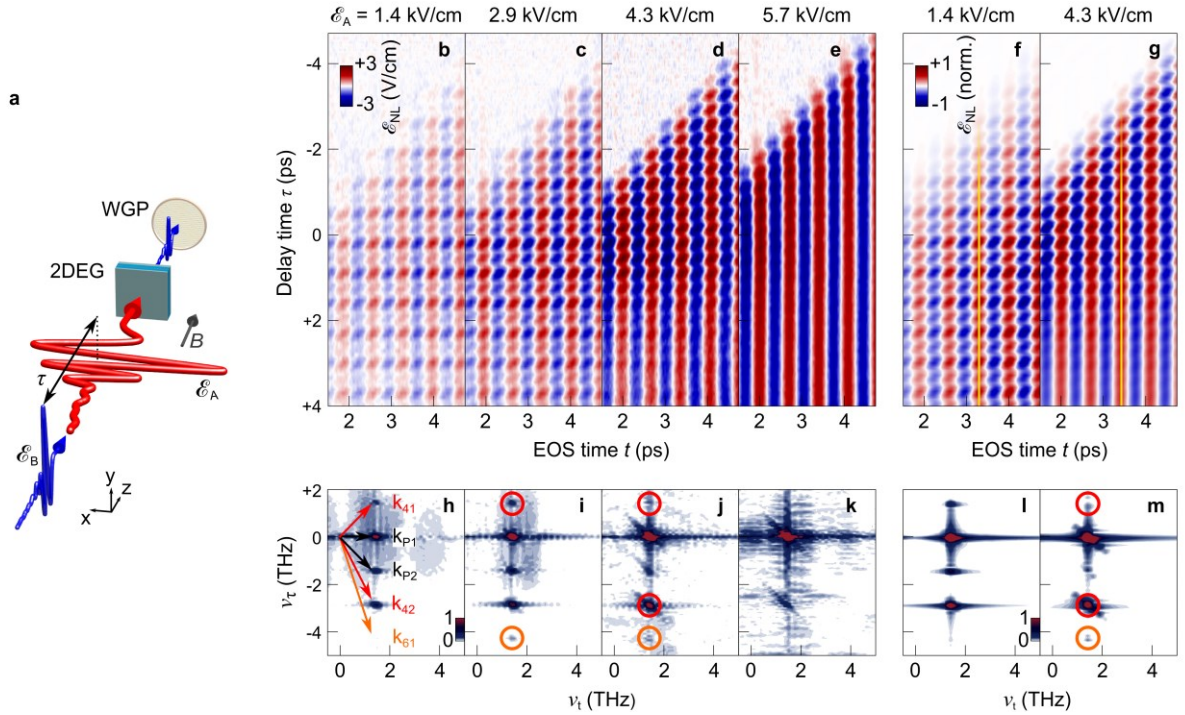


Figure 3 | Two-dimensional, phase-resolved, collinear THz spectroscopy. **a**, Schematic: Strong THz pulses A of amplitude \mathcal{E}_A (polarized in x-direction) prepare a coherent inter-LL polarization in the 2DEG. The nonlinear THz response $\mathcal{E}_{NL}(t, \tau)$ is time-resolved using weak pulses B of amplitude $\mathcal{E}_B = 90$ V/cm (polarized in y-direction), incident after a relative delay time τ . **b-e**, $\mathcal{E}_{NL}(t, \tau)$ for $\mathcal{E}_A = 1.4 - 5.7$ kV/cm. **h-k**, Two-dimensional Fourier transform of $\mathcal{E}_{NL}(t, \tau)$ from **b-e**. Labels and circles highlight spectral positions of coherent pump-probe (k_{p1} , k_{p2} , black), four- (k_{41} , k_{42} , red) and six-wave-mixing nonlinearities (k_{61} , orange), and arrows visualize wave vectors perpendicular to phase fronts of the respective processes. **f,g** and **l,m**, $\mathcal{E}_{NL}(t, \tau)$ and corresponding spectra calculated through a microscopic quantum theory for two representative amplitudes, $\mathcal{E}_A = 1.4$ kV/cm, and $\mathcal{E}_A = 4.3$ kV/cm. Vertical yellow lines indicate the sampling time of $t = 3.3$ ps for which \mathcal{E}_{NL} is analyzed in Fig. 4.

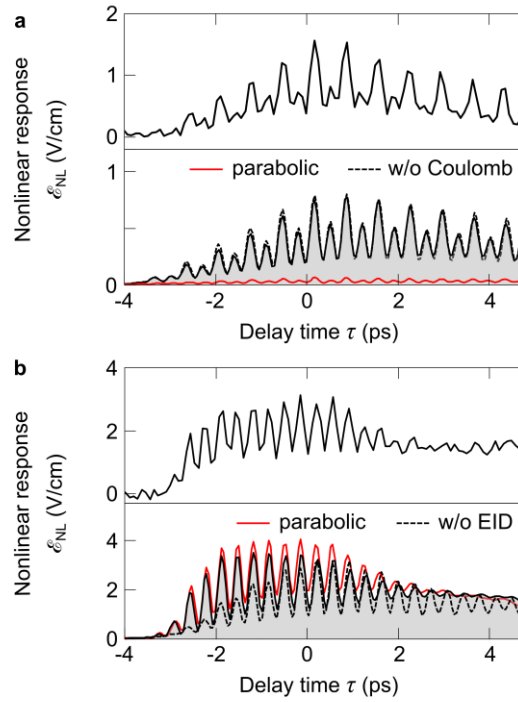


Figure 4 | Time-domain switch-off analysis of nonlinear contributions. **a**, Nonlinear response $\mathcal{E}_{\text{NL}}(t, \tau)$ for $\mathcal{E}_A = 1.4$ kV/cm at a constant sampling time of $t = 3.3$ ps as measured (top panel). Bottom panel: Calculation via a full quantum theory (black curve and shaded area). Dashed curve: calculation excluding Coulomb interaction. Red curve: calculation assuming a parabolic band. **b**, $\mathcal{E}_{\text{NL}}(t, \tau)$ for $\mathcal{E}_A = 4.3$ kV/cm. Top panel: experiment. Bottom panel: full calculation (black curve and shaded area), calculation assuming a parabolic band (red curve), and calculation neglecting excitation-induced dephasing (dashed curve).

Methods

Experiment.

Our sample, grown by molecular beam epitaxy, hosts two 30-nm wide GaAs quantum wells separated by a 10-nm wide $\text{Al}_{0.24}\text{Ga}_{0.76}\text{As}$ barrier. In the 2DEGs, a carrier density $\rho_e = 1.6 \times 10^{11} \text{ cm}^{-2}$ per 2DEG is realized by two remote δ -doping layers, symmetrically enclosing the 2DEGs on both sides. $\text{Al}_{0.24}\text{Ga}_{0.76}\text{As}$ spacers of 72 nm thickness serve as barriers between the 2DEGs and the doping layers (see Supplementary Discussion 2). The resulting high confinement potential for the electrons of 220 meV and the symmetric layout yield two independent electron gases with a high electron mobility of $\mu = 4.6 \times 10^6 \text{ cm}^2/\text{Vs}$, as verified through van der Pauw measurements.

A Ti:sapphire laser amplifier (centre wavelength: 800 nm, pulse energy: 5.5 mJ, repetition rate: 3 kHz, pulse duration: 33 fs) is used to generate intense few-cycle THz fields by tilted-pulse-front optical rectification in a cryogenically cooled LiNbO_3 crystal²³. In a second optical branch, a small portion of the laser energy drives optical rectification in a 180- μm -thick (110)-cut GaP crystal. Both THz pulses are collinearly focused onto the sample which is mounted in a magneto-optical cryostat at a constant temperature of 4.3 K. The superconducting magnet provides homogeneous fields which are polarized perpendicularly to the quantum well plane and are tunable between 0 and 5 T. The transmitted THz pulses pass a rotatable wire-grid polarizer and are focused onto a 0.5-mm-thick (110)-cut ZnTe crystal for polarization-resolved electro-optic detection covering the frequency window between 0.1 and 3.0 THz. Two mechanical delay stages allow us to independently vary the delay time τ between the maxima of the two THz transients labelled A and B, and the electro-optic sampling time t . Differential detection is employed through two mechanical choppers individually modulating the pulses at sub-harmonics of the laser repetition rate, which allows us to clearly isolate feeble THz electric fields of less than 0.1 V/cm from a background on the order of 10 kV/cm (c.f. Supplementary Discussion 3 for details).

Theory.

We describe Landau electrons in the static magnetic field using the minimal substitution Hamiltonian

$$\hat{H} = \frac{1}{2m_e} (\hat{\mathbf{p}} + |e|A_{\text{stat}}(\mathbf{r}))^2, \quad (2)$$

where m_e is the effective electron mass and e denotes the elementary charge. The vector potential A_{stat} is employed in the symmetric gauge and contains the magnetic bias perpendicular to the sample surface. The Hamiltonian (2) yields the Landau wavefunctions, cyclotron frequency, and characteristic length scales on which we base our many-body theory. The full many-body Hamiltonian

$$\hat{H} = \hat{H}_{\text{LL}} + \hat{H}_{\text{ee}} + \hat{H}_{\text{ion}} + \hat{H}_{\text{lm}} \quad (3)$$

contains the non-interacting contributions \hat{H}_{LL} into which we incorporate trivial bandstructure effects, and the interaction term \hat{H}_{lm} describing the light–matter coupling. The complex electron–electron and electron–ion interactions, fully described in Supplementary Discussion 4, are implemented through

$$\hat{H}_{\text{ee}} = \frac{1}{2} \sum_{\substack{n,l,n',l' \\ m,j,m',j'}} V_{m'j',n'l'}^{nl,mj} a_{n,l}^\dagger a_{m,l}^\dagger a_{m',j'} a_{n',l'} \quad (4)$$

$$\hat{H}_{\text{ion}} = -\rho_{\text{ion}} \pi r_c^2 \sum_{n,l,n',l',j} V_{0j,n'l'}^{nl,0j} a_{n,l}^\dagger a_{n',l'}. \quad (5)$$

Here, $a_{n,l}^\dagger$ and $a_{n,l}$ represent the creation and annihilation, respectively, of Landau electrons with principal quantum number n and angular momentum l in the basis determined through Eq. (3), ρ_{ion} is the uniformly distributed positive charge density originating from the dopant ions, and r_c is the radius of the classical Landau orbit. The Coulomb matrix elements V are at the core of the many-body dynamics of the highly excited Landau system and define the numerical challenge, linking electrons in Landau levels through 2.25×10^6 THz-induced transition amplitudes. We solve these dynamics via the semiconductor Bloch equations (SBEs)³ which yield the relevant experimental quantities such as the polarization and occupation densities, accounting for LO phonon scattering as well as EID as fully detailed in Supplementary Discussion 10 together with the explicit form of the SBEs. We propagate the related integro-differential equations with a fourth-order Runge–Kutta method requiring more than

10^{10} calculations due to the Coulomb coupling for each time step, which makes the simulations extremely demanding. Nevertheless, this formidable challenge is executable via an efficient parallel-computing implementation. To study the limitations of Kohn's theorem, we also perform a classical calculation with a nonparabolic energy dispersion and a constant decay, the details of which are given in Supplementary Discussion 4.